Single-ion anisotropy driven chiral magnetic order in a spin-1 antiferromagnetic chain

S. Vaidya,[1,*] S. P. M. Curley,[1] P. Manuel,[2] J. Ross Stewart,[2] M. Duc Le,[2] A. Hernández-Melián,[3] T. J. Hicken,[3,4] C. Wang,[4] H. Luetkens,[4] J. Krieger,[4] S. J. Blundell,[5] T. Lancaster,[3] K. A. Wheeler,[6] D. Y. Villa,[7,8] Z. E. Manson,[7] J. A. Villa,[7] J. L. Manson,[7,†] J. Singleton,[8] R. D. Johnson,[9,10] and P. A. Goddard[1,‡]

[1]*Department of Physics, University of Warwick, Gibbet Hill Road, Coventry CV4 7AL, United Kingdom*
[2]*ISIS Pulsed Neutron Source, STFC Rutherford Appleton Laboratory, Didcot, Oxfordshire OX11 0QX, United Kingdom*
[3]*Department of Physics, Durham University, Durham DH1 3LE, United Kingdom*
[4]*Center for Neutron and Muon Sciences, Paul Scherrer Institut, Forschungsstrasse 111, 5232 Villigen PSI, Switzerland*
[5]*Department of Physics, Clarendon Laboratory, University of Oxford, Parks Road, Oxford OX1 3PU, United Kingdom*
[6]*Department of Chemistry, Whitworth University, Spokane, Washington 99251, USA*
[7]*Department of Chemistry and Biochemistry, Eastern Washington University, Cheney, Washington 99004, USA*
[8]*National High Magnetic Field Laboratory (NHMFL), Los Alamos National Laboratory, Los Alamos, New Mexico, USA*
[9]*Department of Physics and Astronomy, University College London, Gower Street, London WC1E 6BT, United Kingdom*
[10]*London Centre for Nanotechnology, University College London, London WC1H 0AH, United Kingdom*

(Received 8 September 2025; revised 9 April 2026; accepted 16 June 2026; published 3 August 2026)

Chirality in magnetic systems gives rise to a wide range of exotic phenomena, yet its influence in $S = 1$ chains remains largely unexplored. Herein, we present a comprehensive experimental study of a chiral antiferromagnetic $S = 1$ chain, $[Ni(pym)(H_2O)_4]SO_4 \cdot H_2O$ (pym = pyrimidine), where the Ni(II) octahedral orientation exhibits a fourfold chiral periodicity. Muon-spin rotation measurements indicate the onset of long-range magnetic order below $T_N = 1.82(1)$ K. Neutron diffraction measurements reveal a chiral antiferromagnetic order driven by a chiral modulation of the easy-axis anisotropy direction, rather than the typical scenario of Dzyaloshinskii-Moriya interactions, geometrical frustration, or higher-order interactions. Inelastic neutron scattering measurements reveal dispersive spin-wave excitations well described by linear spin-wave theory, with Hamiltonian parameters $J_0 = 6.81(1)$ K (intrachain exchange), $J'_{1a} = -0.09(1)$ K (interchain exchange), and $D = -3.02(1)$ K (easy-axis single-ion anisotropy). These parameters are further validated by Monte Carlo simulations of the magnetization. Additionally, the inelastic neutron scattering data reveal multiple dispersionless bands, suggesting the presence of further excitations beyond the scope of our linear spin-wave theory.

DOI: 10.1103/2gnf-lrdx

I. INTRODUCTION

Chirality arises when an object lacks inversion symmetry, preventing it from being superimposed onto its mirror image. This fundamental concept plays a pivotal role across various scientific disciplines, from the behavior of elementary particles to the handedness of biological molecules. In condensed matter physics, chirality is at the heart of numerous exotic electronic, magnetic, and optical phenomena [1]. Notable examples include chiral fermions in topological Weyl semimetals [2], magnetic chiral dichroism in systems with chiral magnetic order [3–6], skyrmions [7–9], and the topological Hall effect [10]. These effects have drawn considerable interest in recent years, not only for their potential applications in emerging technologies but also for their impact on advancing fundamental physics [8,11–14].

In magnetic systems, chiral order [15] typically emerges due to the Dzyaloshinskii-Moriya interaction in noncentrosymmetric materials. In contrast, chirality in centrosymmetric systems often relies on geometrical frustration or higher-order interactions, such as biquadratic exchange [16–18]. However, these mechanisms are typically weak and challenging to control, especially in $3d$ transition metal systems where spin-orbit coupling is generally small [19]. Moreover, the influence of chirality on low-dimensional quantum spin systems, particularly integer spin systems that can host the Haldane phase, remains largely unexplored.

To address these gaps, we investigate $[Ni(pym)(H_2O)_4]SO_4 \cdot H_2O$ (pym = pyrimidine, $C_4H_4N_2$), an antiferromagnetic $S = 1$ chain where the orientation of the Ni(II) octahedral environment has a fourfold chiral periodicity. In this system the single-ion anisotropy direction is expected to follow the chiral modulation of the Ni(II) octahedra. In systems where the single-ion anisotropy direction alternates between neighboring ions, such as the $S = 1$ staggered chain $Ni(pym)(H_2O)_2(NO_3)_2$ [20], it

*Contact author: shroya.vaidya@npl.co.uk
†Deceased 7 June 2023.
‡Contact author: p.goddard@warwick.ac.uk

Published by the American Physical Society under the terms of the Creative Commons Attribution 4.0 International license. Further distribution of this work must maintain attribution to the author(s) and the published article's title, journal citation, and DOI.

has been shown that an easy-axis anisotropy will result in significant spin canting even without considering the Dzyaloshinskii-Moriya interaction [21,22]. The resulting canting angle is strongly dependent on D/J_0, where D is the single-ion anisotropy energy and J_0 is the exchange interaction strength along the chain. In contrast, in the twofold-staggered *easy-plane* case, intersection of two easy-planes is expected to result in collinear order along a *pseudoeasy axis* [23–25]. A chiral single-ion anisotropy direction may induce a chiral magnetic structure in the absence of the Dzyaloshinskii-Moriya interaction.

Furthermore, a change from a twofold staggered to a chiral structure may have a significant influence on the spin excitations. In the twofold staggered Cu(II) $S = 1/2$ chains, $Cu(C_6D_5COO)_2 \cdot 3D_2O$ and $Cu(pym)(H_2O)_2(NO_3)_2$, the alternating orientation of the local spin environment gives rise to nontrivial staggered g tensors and Dzyaloshinskii-Moriya interactions which, on application of an external magnetic field, generate a staggered field and an energy gap with a $\Delta \sim H^{2/3}$ field dependence [26–28]. It was shown that mapping the Hamiltonian to the sine-Gordon quantum-field theory [29–31] accounts for this behavior and the rich excitation spectra containing soliton and breather modes in the staggered $S = 1/2$ chain. In the $S = 1/2$ chiral chain, $[Cu(pym)(H_2O)_4]SiF_6 \cdot H_2O$ [32], the fourfold periodicity of the octahedral environment was found to result in a linear field dependence of the spin gap, which deviated from theoretical predictions and remains to be fully explained [32].

Here, to investigate the influence of chirality on the magnetic order and spin dynamics in a $S = 1$ chain, we present a comprehensive experimental study of $[Ni(pym)(H_2O)_4]SO_4 \cdot H_2O$. We first confirm the chiral chain structure using single-crystal x-ray diffraction (XRD) and infer the magnetic Hamiltonian. Muon-spin rotation (μ^+SR) measurements show clear signs of long-range magnetic order at low temperatures. Using elastic neutron diffraction, we indeed find an antiferromagnetic chiral order consistent with an easy-axis anisotropy. Inelastic neutron scattering (INS) is then used to quantify the Hamiltonian parameters. Although the dispersive spin-wave excitations are largely accounted for by linear spin-wave theory, there are multiple dispersionless bands which hint at the presence of additional excitations not captured by our linear spin-wave theory model. Finally, we perform classical Monte Carlo simulations of the field-dependent magnetization $M(H)$ to confirm the model determined using inelastic neutron scattering data and linear spin-wave theory simulations.

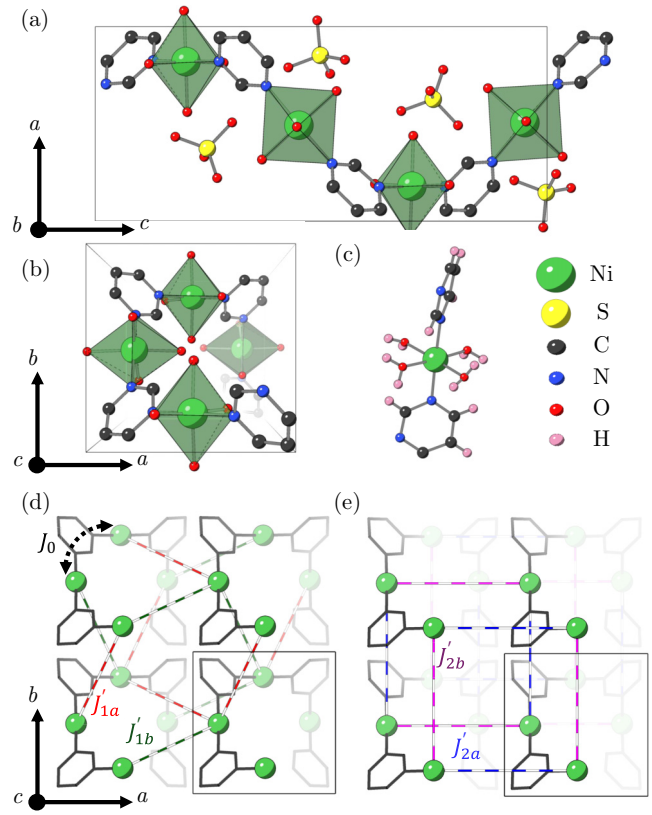


FIG. 1. The structure and exchange pathways of the $S = 1$ chiral chain in $[Ni(pym)(H_2O)_4]SO_4 \cdot H_2O$. (a) View looking down the b axis containing a single chiral chain connected by J_0 exchange mediating pym molecules (H atoms and H_2O molecules have been omitted for clarity). (b) View looking down the tetragonal $P4_1$ unit cell c axis depicting the fourfold rotation of the local Ni(II) octahedral environment. (c) The local crystal environment of each Ni(II) ion. (d) and (e) View down the c axis showing exchange pathways. The black dashed arrow represents the intrachain J_0 pathway. The red and green labeled dashed lines in (d) indicate the J'_{1a} and J'_{1b} interchain exchange interaction, respectively. In (e) the blue and purple labeled dashed lines denote the J'_{2a} and J'_{2b} interchain exchange interaction, respectively. The solid black lines indicate the unit cell boundaries.

II. RESULTS AND DISCUSSION

A. X-ray diffraction

Single-crystal XRD measurements at $T = 100(1)$ K reveal that $[Ni(pym)(H_2O)_4]SO_4 \cdot H_2O$ crystallizes in the chiral space group $P4_1$, with lattice parameters $a = 7.9395(4)$ Å and $c = 18.4594(10)$ Å. As depicted in Fig. 1, the Ni(II) ions are connected by pym ligands, forming Ni-pym-Ni chains that extend along the c axis. Each Ni(II) ion resides in a distorted octahedral environment [see Fig. 1(c)], defined by four equatorial bonds to O donors from H_2O molecules, with Ni-O bond lengths ranging from 2.060(3) Å to 2.078(3) Å and two axial bonds to nitrogen atoms of the pym ligands, with Ni-N bond lengths 2.079(3) Å and 2.087(3) Å. The axial Ni-N bonds are tilted by $\alpha = 49.26(8)^\circ$ relative to the c axis. Additionally, the 4_1 screw axis of the space group induces a 90° counterclockwise rotation about c in the Ni-N bond direction between neighboring Ni(II) ions connected by pym ligands. This results in a chiral chain structure, in which the orientation of the Ni(II) octahedra exhibits a fourfold chiral modulation along the chain [see Fig. 1(b)].

The crystal structure of the chiral chain provides a basis for inferring the model spin Hamiltonian. The dominant antiferromagnetic exchange interaction is expected to occur through the pym ligands with an interaction strength J_0 [20,22,25]. Since the J_0 exchange interaction pathways are not located at inversion centers, Dzyaloshinskii-Moriya interaction terms are also permitted, with the Dzyaloshinskii-Moriya vector having a uniform component along the c axis and a

fourfold staggered component in the *ab* plane [32]. However, in molecule-based Ni(II) systems, the Dzyaloshinskii-Moriya interaction is expected to be small relative to the leading terms in the Hamiltonian [19,22,25]. Indeed, in similar pym-containing Ni(II) systems, we have found that the Dzyaloshinskii-Moriya interaction is not necessary to account for the ground-state magnetic properties [20,25].

Additionally, each Ni(II) ion is coupled to eight neighboring ions in adjacent chains via the four H-bond mediated exchange pathways illustrated in Figs. 1(d) and 1(e). The J'_{1a} and J'_{1b} interactions couple the i^{th} spin in one chain to the $i \pm 1^{\text{th}}$ spins in the adjacent chain, with Ni-Ni distances of 7.5985(6) Å and 7.4852(6) Å, respectively. In contrast, the J'_{2a} and J'_{2b} interactions couple two spins located at the i^{th} position in adjacent chains, with Ni-Ni distances of 7.9395(5) Å. If either J'_{1a} or J'_{1b} share the same sign as J'_{2a} or J'_{2b}, these interchain interactions will compete with each other, resulting in reduced net interchain coupling. Whatever their sign, these interchain interactions are expected to be weak compared to J_0.

The crystal field of the Ni(II) octahedral environment introduces an single-ion anisotropy term in the Hamiltonian. In the local frame of the Ni(II) octahedra, defined such that the z axis aligns with Ni-N bond, the single-ion anisotropy tensor is $K_i^{\text{loc}} = \text{diag}[0, 0, D]$. Here D represents the uniaxial anisotropy parameter. Although the point group symmetry permits rhombohedral anisotropy within the Ni-O plane, variations in the equatorial Ni-O bond lengths are minimal ($< 1\%$), implying that the in-plane anisotropy (E) is negligible compared to D and therefore the anisotropy is assumed to be predominantly uniaxial. Euler rotations are applied to transform K_i^{loc} to the xyz laboratory frame single-ion anisotropy tensor K_i as shown in the Supplemental Material [33].

The spin Hamiltonian of the chiral chain can therefore be written as

$$\mathcal{H} = J_0 \sum_i \hat{\mathbf{S}}_i \cdot \hat{\mathbf{S}}_{i+1} + \sum_{\langle i,j \rangle_\perp} J'_{i,j} \hat{\mathbf{S}}_i \cdot \hat{\mathbf{S}}_j + \sum_i \hat{\mathbf{S}}_i \cdot K_i \cdot \hat{\mathbf{S}}_i + \sum_i g\mu_B \mu_0 \mathbf{H} \cdot \hat{\mathbf{S}}_i, \quad (1)$$

where $\hat{\mathbf{S}}_i$ is the spin operator at site i and $\langle i, j \rangle_\perp$ denotes a sum over unique interchain exchange bonds with strength $J'_{i,j}$. The final term in Eq. (1) describes the Zeeman energy in an applied magnetic field $\mathbf{H}$ and assuming an isotropic g factor. For Ni(II) ions in a slightly distorted octahedral environment, a small g anisotropy may arise, with magnitude $\Delta g = g_z - g_{xy} = 2D/\lambda$, where $\lambda \sim 500$ K is a typical value of the spin-orbit coupling parameter [34]. In Ni(II) systems with similar local environments, $D \sim 10$ K [35], yielding a tiny g-anisotropy $\Delta g \sim 0.04$.

B. Magnetometry

Figure 2 shows the temperature-dependent zero-field-cooled magnetic susceptibility, $\chi(T)$, which was measured in an applied field of 0.1 T using a partially deuterated powder sample of $[Ni(pym)(D_2O)_4]SO_4 \cdot D_2O$, where H in the H_2O molecules were replaced with D atoms. Deuteration of the system was found to have minimal effects on the magnetic properties, as evidenced by the $\chi(T)$ data shown in the Supplemental Material [33]. The field-cooled susceptibility data are also shown in the Supplemental Material [33] and are identical to the ZFC data within experimental uncertainty.

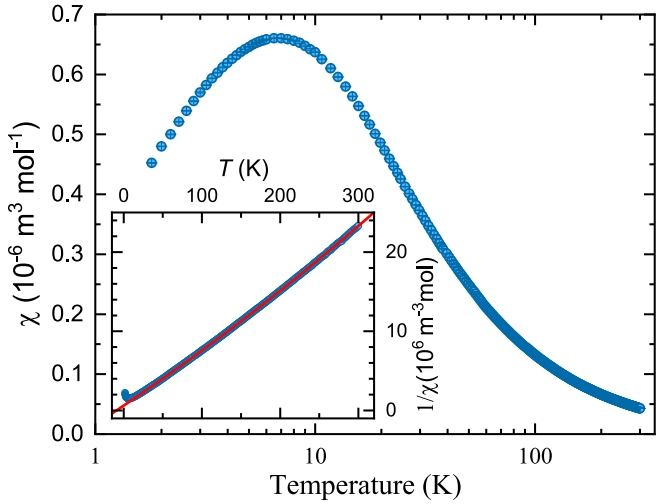


FIG. 2. Zero-field-cooled temperature-dependent magnetic susceptibility, $\chi(T)$, (blue circles) measured on powder samples of the $S = 1$ chiral chain, $[Ni(pym)(H_2O)_4]SO_4 \cdot D_2O$ in an applied field of 0.1 T. Inset: The inverse susceptibility χ^{-1} with a Curie-Weiss fit (red line).

The inset to Fig. 2 presents the inverse susceptibility $\chi^{-1}(T)$. Above 50 K, the ZFC $\chi(T)$ is well described by the Curie-Weiss law, $\chi(T) = C/(T - \theta_{\text{CW}}) + \chi_0$, where the Curie constant $C = N_A \mu_0 g^2 \mu_B^2 S(S+1)/3k_B$ and θ_{CW} is the Curie-Weiss temperature. The temperature-independent term, χ_0, accounts for the paramagnetic Van Vleck contribution from Ni(II) atoms as well as core electron diamagnetism of all atoms in the sample and sample holders [36,37]. Below 15 K, there is an upturn in $\chi^{-1}(T)$ due to the low-temperature suppression of $\chi(T)$ arising from the combination of single-ion anisotropy and strong antiferromagnetic exchange.

A fit to χ^{-1} yields $g = 2.18(1)$, $\chi_0 = -5.73(4) \times 10^{-9}$ $\text{m}^3\text{mol}^{-1}$ and $\theta_{\text{CW}} = -9.19(6)$ K. The g factor is typical of Ni(II) spin-1 systems, and the negative θ_{CW} is indicative of antiferromagnetic coupling between spins bridged by pym. Below 50 K, a broad maximum in $\chi(T)$ is observed at around $T_{\chi\text{max}} \sim 6.5$ K due to the the development of antiferromagnetic short-range correlations along the chain, a common feature in quasi-low-dimensional systems [36,38–42].

Pulsed-field magnetization, $M(H)$, measurements were performed on multiple crystallites coaligned along the chain axis to obtain data with the field applied parallel and perpendicular to the chain, as shown in Figs. 3(a) and 3(c), respectively. For the $H \perp c$ measurements, the crystallites were orientated such that the applied field was close to the crystallographic [1 0 0] direction.

Figures 3(b) and 3(d) display the corresponding differential susceptibilities, $\text{d}M/\text{d}H$. When the field is applied parallel to the chain, a sharp peak in $\text{d}M/\text{d}H$ is observed at $\mu_0 H_{\text{SF}} = 3.30(5)$ T and a temperature of 0.63(1) K, indicative of a spin-flop transition. This transition is no longer present in the $M(H)$ data for $T \geqslant 3.89$ K. At 13.91(5) T, another peak

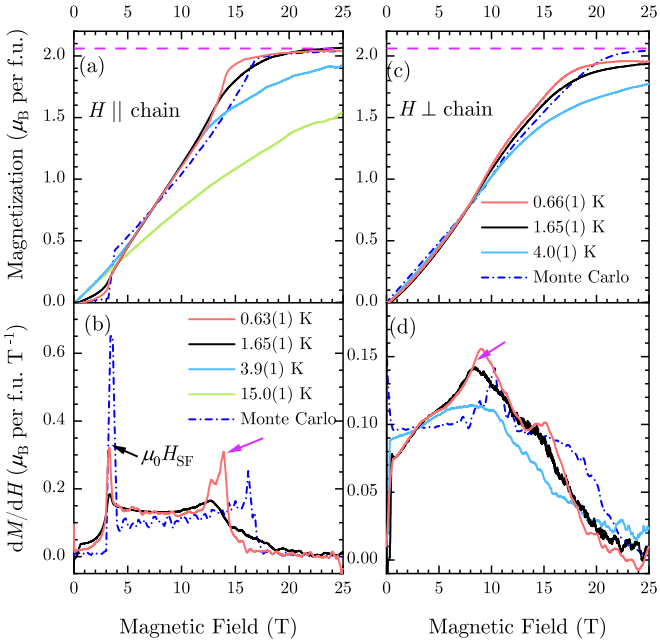


FIG. 3. Field-dependent magnetization, $M(H)$, of chiral $S = 1$ chain $[Ni(pym)(H_2O)_4]SO_4 \cdot H_2O$ with the applied field (a) parallel and (c) perpendicular to the chain. Differential susceptibility, dM/dH, with applied field (b) parallel and (d) perpendicular to the chain. The purple dashed line shows the 0.63(1) K projected saturation value with $H||c$. The black arrow marks the spin-flop transition and the purple arrows indicate additional metamagnetic transitions. The blue dash-dot line in all panels shows the results of the classical Monte Carlo simulation described in Sec. II F.

in dM/dH suggests magnetic saturation. However, $M(H)$ continues to increase gradually up to the projected value of $2.06(2)\,\mu_B$ per Ni(II) ion, as indicated by the purple line in Fig. 3(a). When the field is applied perpendicular to the chain, a peak in dM/dH is observed at 8.9(5) T, suggesting a metamagnetic transition. As the field increases, the magnetization rises gradually to a projected value of $1.95(2)\,\mu_B$ per Ni(II) ion, with no evidence of a magnetic saturation transition. These observations and the Monte Carlo simulations of $M(H)$ are discussed further in Sec. II F.

C. Muon-spin rotation

Zero-field (ZF) μ^+SR measurements were performed on powder samples of $[Ni(pym)(H_2O)_4]SO_4 \cdot H_2O$ using the FLAME instrument at the Swiss Muon Source, Paul Scherrer Institut, Switzerland. A representative ZF μ^+SR spectrum at $T = 0.20(1)$ K is shown in Fig. 4(a). The data show clear oscillations in the time-dependent asymmetry, $A(t)$, indicative of coherent muon-spin precession in a quasistatic local field arising from long-range magnetic order. We find that the spectra in the magnetically ordered regime are well described by two relaxing oscillation components arising from two magnetically distinct μ^+ stopping sites within the sample. Consequently, $A(t)$ can be fitted using a function of the form

$$A(t) = \sum_{i=1}^{2} A_i \cos(2\pi \nu_i t + \phi_i) e^{-\lambda_i t} + A_3 e^{-\lambda_3 t} + A_b. \quad (2)$$

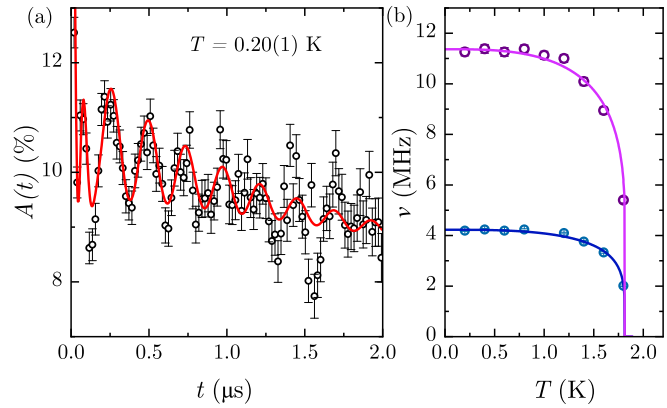


FIG. 4. (a) Representative μ^+SR spectra (black circles) measured at $T = 0.20(1)$ K. (b) Temperature dependence of the muon spin precession frequencies (circles). Solid lines in both correspond to the fits to the data described in the text.

Here, A_b is a contribution from muons stopping in environments where the muon spin is not relaxed, such as nonmagnetic sites and regions outside the sample. The A_i are the magnitudes of each component with corresponding oscillation frequencies ν_i, relaxation rates λ_i, and phase factors ϕ_i. The second term, with amplitude A_3, describes a decaying signal from muons whose polarization is initially parallel to the local magnetic field.

During fitting, the values of $A_b = 8\,\%$ and $\lambda_3 = 0.55\,\mu s^{-1}$ were found to be temperature-independent, and therefore fixed to their average values. The parameters $A_3 = 2.93(1)\%$, $A_1 = 11.0(1)\%$, $A_2 = 2.17(6)\%$, $\phi_1 = -31(2)^\circ$, $\phi_2 = -20(1)^\circ$, and the frequency ratio $\nu_2/\nu_1 = 2.69(3)$ were fitted globally across all temperatures. Nonzero values of ϕ_i are typically associated with incommensurate magnetic order. However, in molecular systems such as this one, nonzero ϕ_i values are observed even in the presence of commensurate order, and the underlying mechanism remains unclear [43].

The temperature dependence of the ν_i were determined by fitting the data at each temperature, and the results are shown in Fig. 4(b). The frequencies ν_i are proportional to the static local magnetic field at the μ^+ stopping sites. In a magnetically ordered material, this local field reflects the magnitude of the ordered magnetic moment in the sample. Therefore, the temperature dependence of the muon precession frequency tracks the behavior of the magnetic order parameter. The temperature dependence of ν_i are described by a phenomenological function [44]

$$\nu_i(T) = \nu_i(0)\left[1 - \left(\frac{T}{T_N}\right)^{\alpha}\right]^{\beta}. \quad (3)$$

Fitting the data in Fig. 4(b) yields an ordering temperature of $T_N = 1.82(1)$ K and $\beta = 0.19(4)$ for a fixed value of $\alpha = 3$[1].

[1]The exponent α describes the low-temperature behavior of the order parameter, whereas β characterizes its behavior near T_N. For antiferromagnetic systems, α typically lies between 2 and 3. However, in our fitting procedure, α tended to have large nonphysical values. We therefore constrained α to a fixed value of 3.

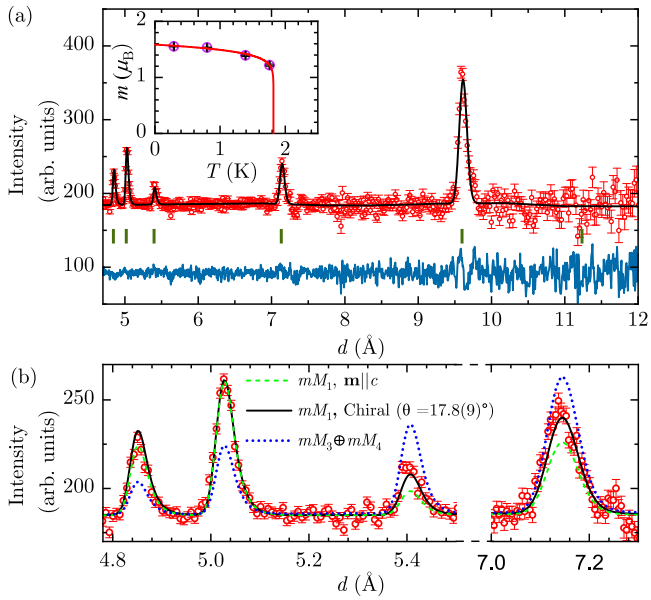


FIG. 5. (a) The magnetic powder diffraction pattern of $[Ni(pym)(D_2O)_4]SO_4 \cdot D_2O$, obtained by subtracting the nuclear structure contribution at 5.0(1) K from the 0.28(1) K data. The red circles represent the data, the black line shows the Rietveld fit of the chiral magnetic structure, the blue line is the difference and the green ticks mark the magnetic Bragg positions. Inset: T dependence of the ordered Ni(II) magnetic moment. (b) Comparison of the diffraction patterns produced by a collinear $m||c$, chiral and $m||ab$ magnetic structures.

Due to the sparse data near T_N, the fitted value of β should not be directly compared to theoretical models.

D. Elastic neutron diffraction

To determine the magnetic structure of the Ni(II) chiral chain below T_N, elastic neutron diffraction experiments were carried out on the WISH instrument at ISIS, the UK Neutron and Muon Source [45,46]. To reduce incoherent background scattering, measurements were carried out on partially deuterated powder samples of $[Ni(pym)(D_2O)_4]SO_4 \cdot D_2O$. Rietveld refinement of the nuclear structure was performed using the FULLPROF software package [47] and reveals that $[Ni(pym)(D_2O)_4]SO_4 \cdot D_2O$ retains the $P4_1$ structure down to $T = 0.28(1)$ K, with the lattice parameters $a = 7.930\,17(16)$ Å and $c = 18.454\,01(66)$ Å, which are close to the values determined using XRD. Further details on the nuclear structure refinement using powder diffraction data can be found in the Supplemental Material [33].

Data were collected above and below T_N, at $T = 5.0(1)$ K and $T = 0.28(1)$ K. Due to the low magnetic scattering cross-section of $S = 1$ moments relative to the nuclear scattering cross-section, the magnetic structure was determined from the difference between the 0.28 and 5 K data, as shown in Fig. 5. The subtracted data reveals several magnetic Bragg reflections which are indexed by the commensurate propagation vector $\mathbf{k} = (1/2, 1/2, 0)$. Symmetry analysis using ISODISTORT [48,49] reveals three candidate symmetries for the magnetic structure: irreducible representation mM_1, mM_2, and $mM_3 \oplus mM_4$. The irreducible representation mM_2 corresponds to ferromagnetic order along the chain and can be ruled out from the negative θ_{CW}.

TABLE I. Magnetic basis vectors, Ψ_i, for the four Ni(II) sites in the unit cell of the $P4_1$ crystal of $[Ni(pym)(D_2O)_4]SO_4 \cdot D_2O$, associated with the magnetic propagation vector $\mathbf{k} = (\frac{1}{2}, \frac{1}{2}, 0)$. The vectors are transformed by the irreducible representations (irreps) mM_1 and $mM_3 \oplus mM_4$, with components (x, y, z) indicating the direction of the magnetic moment at each Ni site.

		Ni sites			
Irrep.	Basis vector	Ni1	Ni2	Ni3	Ni4
mM_1	Ψ_1	(1,0,0)	(0, $\bar{1}$, 0)	($\bar{1}$, 0, 0)	(0,1,0)
	Ψ_2	(0,1,0)	(1,0,0)	(0, $\bar{1}$, 0)	($\bar{1}$, 0, 0)
	Ψ_3	(0,0,1)	(0, 0, $\bar{1}$)	(0,0,1)	(0, 0, $\bar{1}$)
$mM_3 \oplus mM_4$	Ψ_1	(1,0,0)	(0,0,0)	(1,0,0)	(0,0,0)
	Ψ_2	(0,1,0)	(0,0,0)	(0,1,0)	(0,0,0)
	Ψ_3	(0,0,1)	(0,0,0)	(0, 0, $\bar{1}$)	(0,0,0)
	Ψ_4	(0,0,0)	(1,0,0)	(0,0,0)	(1,0,0)
	Ψ_5	(0,0,0)	(0,1,0)	(0,0,0)	(0,1,0)
	Ψ_6	(0,0,0)	(0,0,1)	(0,0,0)	(0, 0, $\bar{1}$)

Table I lists the symmetry-allowed magnetic basis vectors Ψ_i, obtained by projection of the irreducible representations mM_1 and $mM_3 \oplus mM_4$, for the four Ni(II) sites in the $P4_1$ unit cell of $[Ni(pym)(D_2O)_4]SO_4 \cdot D_2O$. The corresponding magnetic basis vectors are illustrated in Fig. 6. The magnetic structure associated with each irreducible representations is a linear combination of these basis vectors with the mixing coefficients c_i ($\sum_i c_i \Psi_i$).

Within the mM_1 irreducible representation, the basis vector Ψ_3 corresponds to an antiferromagnetic mode in which the magnetic moments are aligned along the c axis, with nearest-neighbor Ni(II) ions along each chain coupled antiferromagnetically. In contrast, the basis vectors Ψ_1 and Ψ_2 represent chiral modes confined to the ab plane. For these basis vectors, the in-plane components of the Ni(II) magnetic moments undergo a 90° clockwise rotation between nearest neighbors Ni(II) ions along the chain, as shown in Figs. 6(a) and 6(b). Together, these basis vectors span the physically allowed magnetic degrees of freedom associated with the mM_1 representation. We note a systematic absence of the (1,1,0), (−1, −1, 0), and (−1, 1, 0) magnetic reflections at 11.235 Å. The intensity of this reflection is proportional to c_1, the amplitude of the Ψ_1 basis vector. Therefore, within the noise limits of our data, we conclude that the Ψ_1 basis vector is not present in the magnetic structure associated with the mM_1 irreducible representation. This reduces the number of active degrees of freedom to two, the amplitudes c_2 and c_3. In practice, we refine the ordered magnetic moment size, $m = \sqrt{c_2^2 + c_3^2}$, and the canting angle away from the c axis, $\theta = \arctan(c_2/c_3)$. To test a collinear antiferromagnetic structure described solely by Ψ_3, we fix $\theta = 0$ and allow m to refine freely against the experimental data.

In the $mM_3 \oplus mM_4$ irreducible representation, the magnetic moments of nearest-neighbor spins along the chain are independent, with the basis vectors $\Psi_{1,2,3}$ describing the moments on sites Ni1 and Ni3, and $\Psi_{4,5,6}$ describing

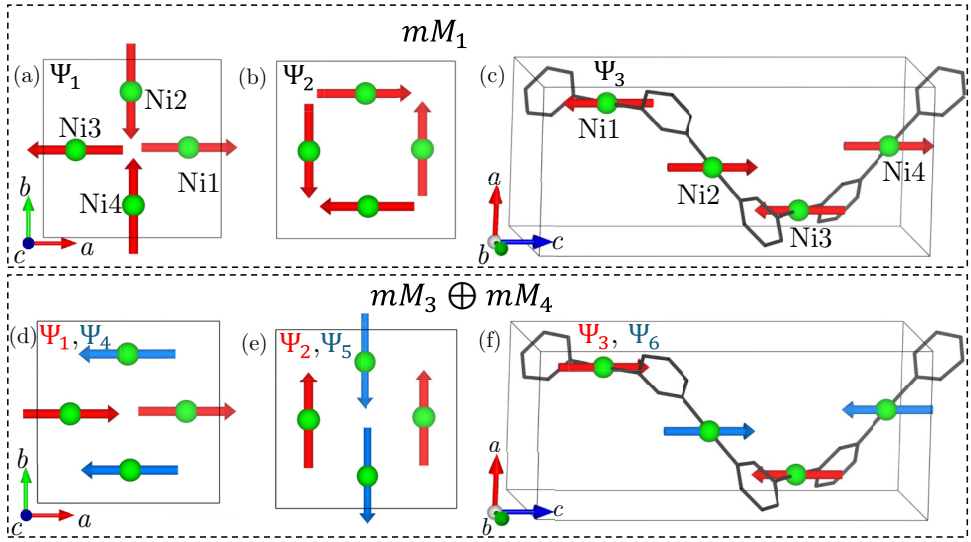


FIG. 6. Magnetic basis vectors Ψ_i transformed by the symmetries of the mM_1 irreducible representation (a)–(c) and the $mM_3 \oplus mM_4$ irreducible representation (d)–(f), shown for the four Ni(II) sites in the $P4_1$ unit cell of $[Ni(pym)(D_2O)_4]SO_4 \cdot D_2O$. Red and blue arrows indicate the magnetic moments and solid black lines show the crystallographic unit cell boundaries.

those on sites Ni2 and Ni4 [see Figs. 6(d)–6(f)]. The basis vectors Ψ_3 and Ψ_6 correspond to collinear magnetic moments aligned along the c axis, with next-nearest-neighbor Ni(II) ions coupled antiferromagnetically. In contrast, the basis vectors $\Psi_{1,2,4,5}$ describe moments in the ab plane, for which the next-nearest neighbors are ferromagnetically coupled. Within this irreducible representation, an antiferromagnetic configuration between nearest neighbors is therefore only possible when the magnetic moments lie in the ab plane and amplitudes of Ψ_3 and Ψ_6 must be zero. Additionally, the ordered magnetic moment size must be equal on all sites. This leaves three degrees of freedom: $m = \sqrt{c_1^2 + c_4^2} = \sqrt{c_2^2 + c_5^2}$, and the in-plane angles $\phi_1 = \arctan(c_1/c_4)$ and $\phi_2 = \arctan(c_2/c_5)$, where ϕ_1 and ϕ_2 describe the moment directions of the Ni1/Ni3 and Ni2/Ni4 sublattices, respectively.

The simulated diffraction patterns corresponding to the different ground states are shown in Fig. 5(b). The intensities of the magnetic reflections are best reproduced by the mM_1 chiral structure with a $R_{mag} = 8.398\%$ compared to $R_{mag} = 11.93\%$ of the collinear ($\theta = 0°$) structure and $R_{mag} = 36.06\%$ of the ab-plane structure within the $mM_3 \oplus mM_4$ irreducible representation. The resulting fit yields $\theta = 17.8(9)°$ and an ordered-moment size of $1.60(1)\,\mu_B$ at $T = 0.28$ K. The refined magnetic structure of $[Ni(pym)(D_2O)_4]SO_4 \cdot D_2O$ is depicted in Fig. 7. Spins cant toward the local Ni-N axes, indicating an easy-axis anisotropy, consistent with our previous report on the nonchiral Ni(II) staggered chain, $Ni(pym)(H_2O)_2(NO_3)_2$, which hosts a similar Ni(II) octahedral environment [20]. The Ni(II) octahedra rotate *counterclockwise* along the chain. In contrast, the ab-plane components of the magnetic moments rotate *clockwise*. This opposite handedness arises solely from antiferromagnetic nearest-neighbor coupling. In contrast, a ferromagnetic structure belonging to the mM_2 symmetry would exhibit the same handedness as the structural rotation.

The suppression of the ordered moment size, from the classical expectation value of $gS \approx 1.99\,\mu_B$ observed at high field, suggests the presence of quantum fluctuations typical of a quasi-low-dimensional system [28,50–52]. The temperature dependence of the ordered magnetic moment $m(T)$ is shown in the inset to Fig. 5(a) and is modeled using a power-law function of the form

$$m(T) = m(0)[1 - (T/T_N)]^{\beta}. \quad (4)$$

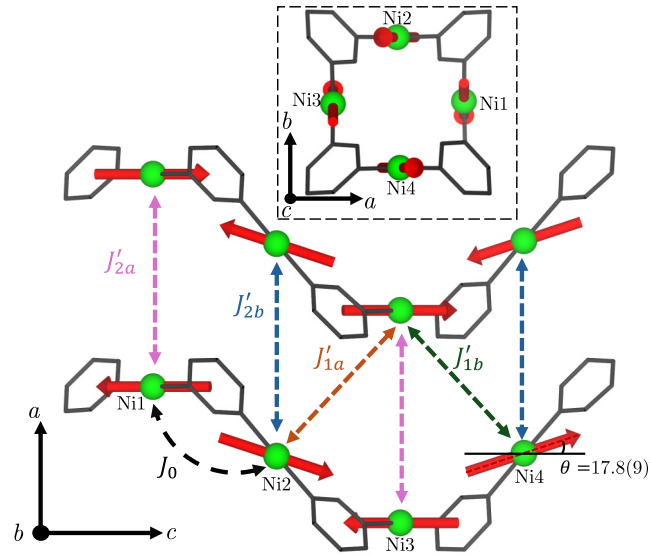


FIG. 7. Zero-field magnetic structure of the $S = 1$ chiral chain $[Ni(pym)(D_2O)_4]SO_4 \cdot D_2O$ determined using elastic neutron diffraction and viewed looking down the b axis. The red arrows indicate the Ni(II) moments which are canted by $\theta = 17.8(9)°$ from the c axis and whose component in the ab plane rotates by 90° from site to site along the chain yielding a chiral magnetic structure. Dashed lines indicate the magnetic exchange interactions. Inset: View of a single chain down the c axis showing chiral arrangement of the magnetic moments.

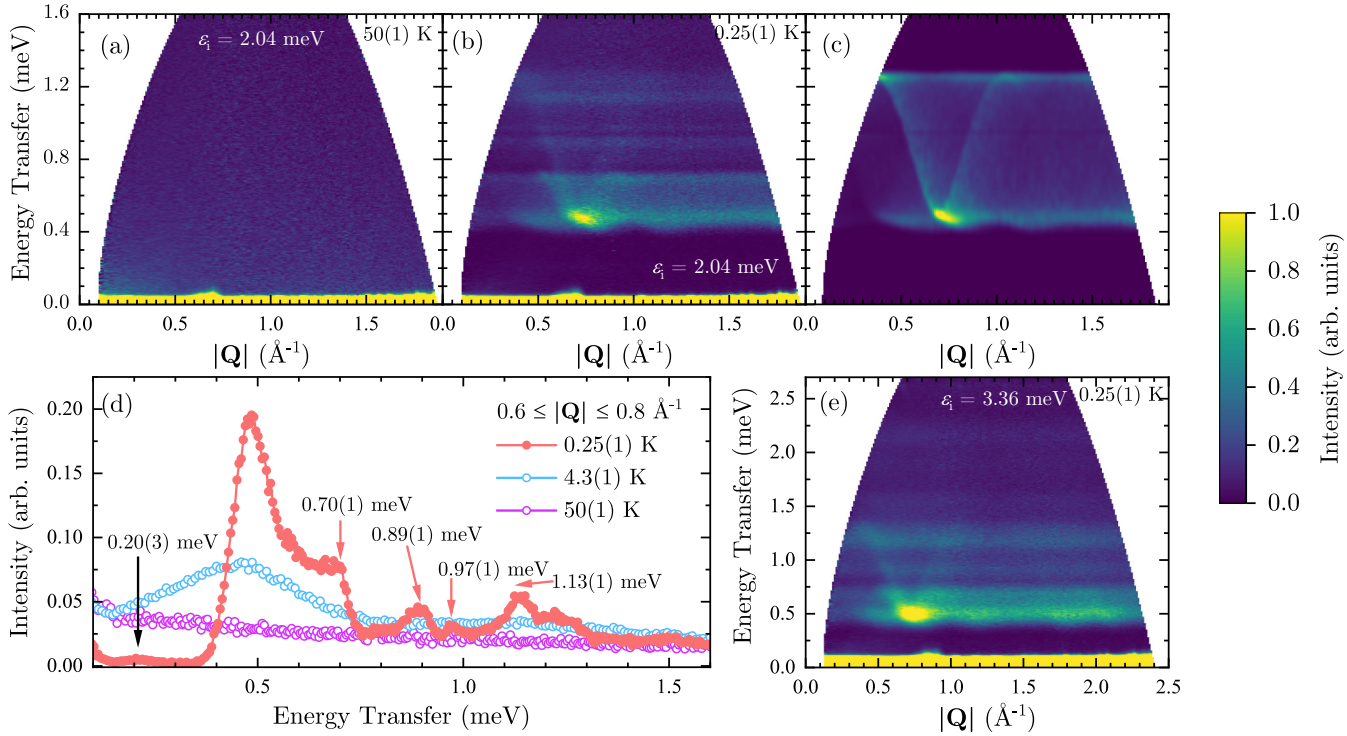


FIG. 8. Time of flight powder inelastic neutron scattering (INS) spectra of $[Ni(pym\text{-}D_4)(H_2O)_4]SO_4 \cdot H_2O$ taken at (a) 50(1) K and (b) 0.25(1) K with $\epsilon_i = 2.04$ meV. (c) Powder averaged linear spin wave theory simulations of the spin-wave spectra using the Hamiltonian in Eq. (1) and the parameters $J_0 = 6.81(1)$ K, $J'_{1a} = -0.09(1)$ K, and $D = -3.02(1)$ K. (d) Line cut of the spectra observed at various temperatures, integrated over $0.6 < |\mathbf{Q}| < 0.8$ Å^{-1}. (e) Inelastic neutron scattering spectra collected at 0.25(1) K with $\epsilon_i = 3.36$ meV.

Fitting the data yields $m(0) = 1.60(3)\,\mu_B$, $\beta = 0.12(5)$, and $T_N = 2.0(2)$ K, in good agreement with the ordering temperature determined from ZF μ^+SR measurements. However, due to the limited number of data points near T_N, the extracted value of β should be interpreted with caution and may not be directly comparable to theoretical critical exponents.

To provide an estimate of the D/J ratio expected to produce a canting angle $\theta = 17.8(9)^\circ$, we can consider a mean-field model containing only the D and J_0 terms in Eq. (1). As derived in the Supplemental Material [33], this model yields the expression

$$\frac{D}{J_0} = \frac{\sin 2\theta}{2\sin(\theta-\alpha)\cos(\theta-\alpha)}. \tag{5}$$

Substituting $\alpha = 49.26(8)^\circ$ and $\theta = 17.8(9)^\circ$ into Eq. (5) yields an estimated ratio of $|D|/J_0 \approx 0.65(4)$, which is reasonably similar to the D/J ratio in other Ni(II) systems [19,22,25].

E. Inelastic neutron scattering

To quantify the Hamiltonian in Eq. (1), inelastic neutron scattering experiments were carried out at 0.25(1) K, 4.3(1) K and 50(1) K on the LET instrument at ISIS with incident energies $\epsilon_i = 2.04$ and 3.36 meV [53,54]. Fully deuterated powder samples of $[Ni(pym\text{-}D_4)(D_2O)_4]SO_4 \cdot D_2O$ were used, where all H atoms in the pym and H_2O ligands were replaced with D.

Inelastic neutron scattering spectra collected with $\epsilon_i = 2.04$ at $T = 50(1)$ and 0.25(1) K are shown in Figs. 8(a) and 8(b), respectively. Figure 8(d) shows the energy cuts of spectra, integrated over $0.6 < |\mathbf{Q}| < 0.8$ Å^{-1} at various temperatures. The 50(1) K data is featureless with the exception of some quasielastic scattering which decays with increasing ϵ, consistent with a paramagnetic state. The 4.3(1) K spectra, shown in the Supplemental Material [33], exhibit a broad $|\mathbf{Q}|$ and ϵ dependent scattering due to short-range correlations along the chain. The observation of short-range correlations at this temperature is consistent with the broad maximum observed in the $\chi(T)$ data.

In the ordered regime, at $T = 0.25(1)$ K, the inelastic neutron scattering data exhibit gapped, dispersive spin-wave excitations [Fig. 8(b)], along with several bright dispersionless bands. These appear as prominent peaks in the $|\mathbf{Q}|$ integrated cuts at 0.70(1), 0.89(1), 0.97(1), and 1.13(1) meV [Fig. 8(d)]. A suppression of intensity is also evident as a dark band between the 0.89(1), 0.97(1) meV peaks at 0.95(1) meV [Fig. 8(b)]. Additionally, a low-intensity in-gap peak is observed in the integrated cuts at 0.20(3) meV. This is reminiscent of the in-gap feature observed in the Ref. [20] and may originate from the transition between the single-ion anisotropy split $|m_s = 0\rangle$ and $|m_s = \pm 1\rangle$ states of impurity Ni(II) ions which are orphaned from the exchange network. This would suggest that $|D| \approx 2.3(3)$ K. In the 0.25 K spectra collected with $\epsilon_i = 3.36$ meV, low-intensity double magnon scattering extends up to 2.2 meV [Fig. 8(e)].

The main dispersive feature extends from the energy gap of 0.4 meV up to the top of the single-magnon band at 1.25 meV. Linear spin-wave theory simulations, as implemented in the SpinW [55] program, and using Eq. (1) reveal

that the 0.4 meV energy gap and bandwidth of the dispersion is determined by a unique combination of J_0 and D values.

A periodic modulation of the energy gap as a function of $|\mathbf{Q}|$ is observed, indicating that low-energy dispersive spin-wave branches exist in this region. Linear spin-wave theory simulations show that this modulation arises from interchain spin-wave dispersions in the plane perpendicular to the chain. As such, the bandwidth of the modulation reflects the overall strength of the net interchain interactions. However, because four distinct interchain exchanges contribute to this gap modulation, it is not possible to uniquely determine the magnitude and sign of each individual exchange. A distinct suppression of intensity at 0.95(1) meV is only reproduced in the simulations when either J'_{1a} or J'_{1b} interactions are the dominant interchain interactions. The shorter hydrogen-bond exchange pathway suggests that $|J'_{1a}| > |J'_{1b}|$, hence J'_{1a} was refined against the data, whereas $J'_{1b} = J'_{2a} = J'_{2b} = 0$ were fixed.

The dispersionless band at 0.70(1) meV is not reproduced by the simulations, even when higher-order interactions are considered. Therefore, to aid in convergence when fitting J_0, D and J'_{1a} parameters, data between 0.6 and 0.75(1) meV were masked. The values of J_0, D, and J'_{1a} were optimized by using the Nelder-Mead simplex algorithm to fit the simulations to the $I(|\mathbf{Q}|, \epsilon)$ 2D map. The resulting simulations, with the fitted parameters $J_0 = 6.81(1)$ K (0.586(9) meV), $J'_{1a} = -0.09(1)$ K (0.0079(8) meV), and $D = -3.02(1)$ K (0.2602(9) meV), are shown in Fig. 8(c) and representative energy cuts with a comparison of the model and the data are shown in Fig. 9. The value of D obtained from the fit is in reasonable agreement with the value implied by the 0.20(8) meV in-gap peak. The single-ion anisotropy parameter used in SpinW simulations is renormalized by a factor $[1 - 1/(2S)]$ to account for the nonlinear contributions to the single-ion anisotropy which are omitted in linear spin-wave theory [56,57]. The results imply a ratio $D/J_0 = 0.443(5)$ and Eq. (5) yields an estimated canting angle of $\theta \approx 12.6^\circ$. These values are smaller than the $D/J_0 = 0.65(4)$ and $\theta = 17.8(9)^\circ$ estimated from the elastic neutron diffraction data. This may indicate that the linear spin-wave theory model over-estimates the value J_0 or underestimates D. Indeed, linear spin-wave theory is a semiclassical technique which is largely successful in predicting spin dynamics in large-S classical systems, whereas in small-S and low-dimensional quantum systems, it can fall short of capturing the full excitation spectra [57–60]. Additionally, linear spin-wave theory neglects higher-order corrections such as magnon-magnon interactions and double magnon scattering, resulting in quantitative disagreements in the spectral weight as seen in Fig. 9. The $S = 1$ Ni(II) spin, low-dimensionality ($|J'_{1a}/J_0| \approx 0.01$), and suppressed ordered moment size present here, indicate a need for more robust spin-wave calculations taking into account additional quantum corrections. It was also recently argued that some details of $S = 1$ systems cannot be captured by conventional spin-wave theory, and instead require a generalized approach in which the local $S = 1$ degrees of freedom is the eight generators of the SU(3) algebra [60]. With this approach, additional features within the dispersive band, similar to that observed in the spectra presented here, were reproduced by the simulations [60]. This is a developing issue that requires further investigation.

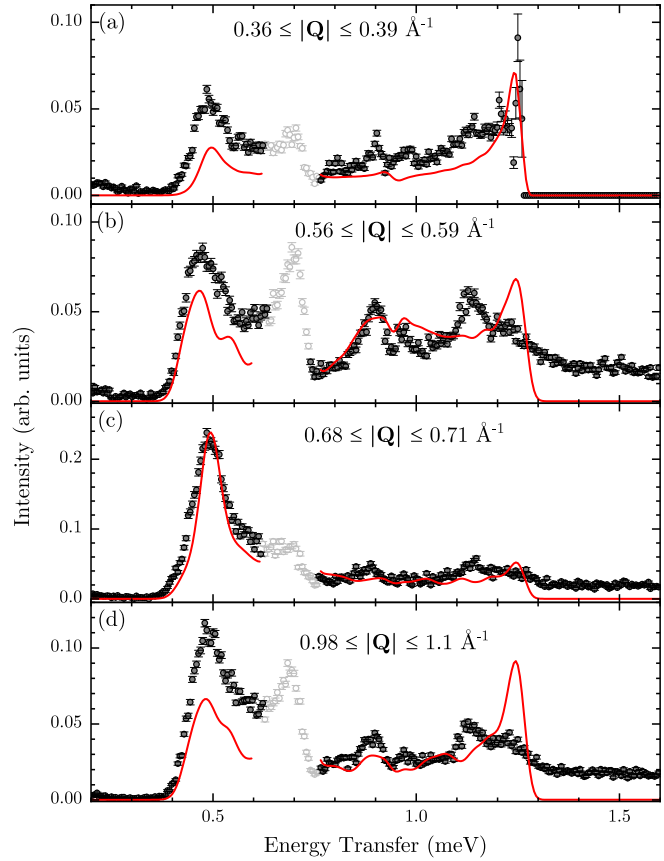


FIG. 9. Representative line cuts of the inelastic neutron scattering data for $[Ni(pym\text{-}D_4)(D_2O)_4]SO_4 \cdot D_2O$. The data are integrated over (a) $0.36 \leqslant |\mathbf{Q}| \leqslant 0.39$ Å^{-1}, (b) $0.56 \leqslant |\mathbf{Q}| \leqslant 0.59$ Å^{-1}, (c) $0.68 \leqslant |\mathbf{Q}| \leqslant 0.71$ Å^{-1}, and (d) $0.98 \leqslant |\mathbf{Q}| \leqslant 1.1$ Å^{-1}. The red lines are modeled using Eq. (1) and the parameters $J_0 = 6.81(1)$ K, $J'_{1a} = -0.09(1)$ K, and $D = -3.02(1)$ K, determined by fitting the full 2D dataset. Data points are shown as black circles, and the gray circles indicate the data masked during fitting.

Nevertheless, the linear spin-wave theory model presented here succeeds in two keys aspects. First, it reproduces the main dispersive features, as demonstrated by comparing the simulated dispersion and the data [see Figs. 8(b) and 8(c)]. Second, it provides a reasonable estimate of the sizes of J_0, D and the net interchain interactions which stabilize the observed chiral magnetic structure. Hence, while more complex and computationally expensive methods may provide additional insights, linear spin-wave theory sufficiently captures the details required for this work.

F. Monte Carlo simulations

To check the Hamiltonian parameters of $[Ni(pym)(H_2O)_4]SO_4 \cdot H_2O$, determined through inelastic neutron scattering experiments, Monte Carlo simulations of the low-temperature $M(H)$ data were performed. For each H value, the spin configuration of a cluster of 16 ions arranged in four chains is determined by minimizing the energy of the system using the Hamiltonian in Eq. (1), with periodic boundary conditions. The resulting simulated $M(H)$ and dM/dH, with

the field applied parallel and perpendicular to the chain, are shown as blue dash-dot lines in Fig. 3.

When the applied magnetic field is aligned parallel to the chain, the spin-flop transition is reproduced at $\mu_0 H_{SF} = 3.5(2)$ T [see Fig. 3(b)]. As the field increases, the simulated $M(H)$ successfully captures the characteristic concave rise observed in the experimental data. However, the high-field peak in dM/dH is predicted to occur at 16.6(2) T, which is higher than the experimentally observed value of 13.91(5) T. Beyond this peak, both the data and the simulations show that $M(H)$ continues to increase with the applied field.

In systems with an alternating single-ion anisotropy axis, there exist principal directions along which the single-ion anisotropy can lower the system's energy by allowing the spins to cant away from the field direction [20,25]. As a result, true magnetic saturation is only achieved in the infinite field limit. In $[Ni(pym)(H_2O)_4]SO_4 \cdot H_2O$, for high fields applied along the c axis ($H \parallel c$), the chiral nature of the single-ion anisotropy axis is expected to give rise to a chiral ferromagnetic phase rather than a fully spin-polarized state. In this phase, the c-axis components of the spin exhibit ferromagnetic alignment, whereas the ab-plane components display a fourfold chiral modulation along the chain, similar to the chiral antiferromagnetic zero-field state. As the field strength approaches infinity, the canting angle θ tends toward zero, resulting in a continued increase in magnetization up to the highest applied fields.

The $H \perp c$ data were best reproduced by the simulation when the applied field is within the ab plane and tilted by roughly 10° from [100] direction [see Figs. 3(c) and 3(d)], which is within the alignment error. The simulated $M(H)$ exhibits a concave rise with increasing field, mirroring the data. Moreover, the broad peak in dM/dH at 8.9(5) T is qualitatively reproduced by the simulation, albeit shifted to a higher field of 10.3(5) T. At fields above 20 T, the simulation begins to overestimate $M(H)$, suggesting the presence of a small g-factor anisotropy. Accurately quantifying this anisotropy would require measurements directly sensitive to the g factor, such as electron spin resonance performed at high excitation frequencies to overcome the effects of zero-field splitting.

Although these simulations capture the overall characteristic of the measured $M(H)$ data well, there are systematic discrepancies between the positions of the salient features, such as the apparent saturation features in Fig. 3(c) and the decrease in dM/dH in Fig. 3(d). These discrepancies suggest that, while the model qualitatively captures the magnetic properties of $[Ni(pym)(H_2O)_4]SO_4 \cdot H_2O$, the D/J_0 value might be slightly underestimated by the linear spin-wave theory model, consistent with earlier discussions.

III. SUMMARY AND CONCLUSIONS

The magnetic properties of the chiral $S = 1$ chain compound $[Ni(pym)(H_2O)_4]SO_4 \cdot H_2O$ have been characterized using a range of experimental techniques. In this system, Ni(II) ions are linked into chains via pym ligands, with the Ni(II) octahedra exhibiting a fourfold chiral modulation in their orientations along the chain. Adjacent chains are connected through complex hydrogen-bonded networks, which are expected to help mediate interchain exchange interactions. These interactions stabilize the three-dimensional long-range magnetic order below $T_N = 1.82(2)$ K, as determined by μ^+SR measurements. Powder neutron diffraction reveals a commensurate chiral antiferromagnetic structure, characterized by antiferromagnetic alignment of the spin components along the c axis and a 90° clockwise rotation of the ab-plane components between neighboring spins.

The Hamiltonian parameters, $J_0 = 6.81(1)$ K, $J'_{1a} = -0.09(1)$ K, and $D = -3.02(1)$ K were determined through linear spin-wave theory analysis of inelastic neutron scattering data. Although this model captures the main features of the spin-wave spectra, it underestimates the canting angle ($\theta \approx 12.6°$ predicted vs $\theta = 17.8(9)°$ observed) and fails to reproduce dispersionless features observed in the spectra. These discrepancies are attributed to limitations of linear spin-wave theory in capturing the physics of low-dimensional, anisotropic quantum systems and highlight the need for the development of a spin-wave model more suited to $S = 1$ quantum spin chains.

Our results demonstrate that the chiral magnetic order in this material does not rely on typically required Dzyaloshinskii-Moriya interactions, geometric frustration, or higher-order exchange mechanisms. Instead, the dominant factor appears to be easy-axis anisotropy, which mirrors the fourfold chiral pattern of the Ni(II) octahedra. Unlike chiral orders induced by other mechanisms, the anisotropy-driven chiral magnetic order observed here is commensurate and rigidly coupled to the underlying crystal chirality. While this mechanism of producing chiral magnetic order precludes the possibility of stabilizing skyrmions, it introduces a new design principle for realizing chiral magnetic materials with potentially robust and tunable properties [1].

Chirality is a key factor in optical phenomena, underpinning effects such as magnetic circular dichroism and magnetochiral dichroism. These effects are enhanced in chiral magnetic systems at the x-ray absorption edges [3,61,62], and have been linked to spin-mediated optical activity [5]. Future work could explore these magneto-optical effects experimentally in $[Ni(pym)(H_2O)_4]SO_4 \cdot H_2O$.

Finally, linear $S = 1$ easy-axis chains with comparable values of $|D|/J_0$ and J'_{1a}/J_0 are expected to exhibit Ising antiferromagnetic order, rather than entering the Haldane phase [63]. In the case of $[Ni(pym)(H_2O)_4]SO_4 \cdot H_2O$, the chirality of the crystal structure imposes a chiral magnetic order through the single-ion anisotropy. Notably, in coordination polymer systems, the D/J_0 ratio can be tuned through external parameters such as applied pressure or chemical modification via ligand substitution [25,52,64–72]. This tunability suggests that the anisotropy-induced chiral magnetic order in $[Ni(pym)(H_2O)_4]SO_4 \cdot H_2O$, and potentially in related $S = 1$ chain systems, could be manipulated to explore the interplay between the Haldane phase and chirality.

ACKNOWLEDGMENTS

We thank the late J.L.M. for instigating this work, contribution to the design and growth of the samples, and for his numerous invaluable contributions. We thank T. Orton

and P. Ruddy for their technical assistance. We also thank R. Coldea, D. M. Pajerowsk, and C. Stock for valuable discussions. S.V. thanks the UK Engineering and Physical Sciences Research Council (EPSRC) for supporting his studentship. This project has received funding from the European Research Council (ERC) under the European Union's Horizon 2020 Research and Innovation Programme (Grant Agreement No. 681260) and EPSRC (Grant No. EP/N024028/1). A portion of this work was performed at the National High Magnetic Field Laboratory, which is supported by National Science Foundation Cooperative Agreements No. DMR-1644779 and No. DMR-2128556, the U.S. Department of Energy (DoE), and the State of Florida. J.S. acknowledges support from the DoE BES FWP "Science of 100 T". We are grateful for the NSF Grant No. CHE-1827313. Part of this work was carried out at the Swiss Muon Source, Paul Scherrer Institut and we are grateful for the provision of beamtime. A.H.-M. is grateful to STFC-ISIS and EPSRC for Ph.D. studentship funding. The work at EWU was supported by the National Science Foundation through Grant No. DMR-2104167. Data presented in this paper will be made available at [73]. The data collected on the WISH and LET instruments can be found in Refs. [46,54] respectively. For the purpose of open access, the author has applied a Creative Commons Attribution (CC-BY) license to any Author Accepted Manuscript version arising from this submission.

DATA AVAILABILITY

The data that support the findings of this article are openly available [46,54,73].

[1] E. Bousquet, M. Fava, Z. Romestan, F. Gómez-Ortiz, E. E. McCabe, and A. H. Romero, Structural chirality and related properties in periodic inorganic solids: Review and perspectives, J. Phys.: Condens. Matter **37**, 163004 (2025).

[2] B. Yan and C. Felser, Topological materials: Weyl semimetals, Annu. Rev. Condens. Matter Phys. **8**, 337 (2017).

[3] M. Saito, K. Ishikawa, K. Taniguchi, and T. Arima, Magnetic control of crystal chirality and the existence of a large magneto-optical dichroism effect in CuB_2O_4, Phys. Rev. Lett. **101**, 117402 (2008).

[4] R. Sessoli, M.-E. Boulon, A. Caneschi, M. Mannini, L. Poggini, F. Wilhelm, and A. Rogalev, Strong magneto-chiral dichroism in a paramagnetic molecular helix observed by hard X-rays, Nat. Phys. **11**, 69 (2015).

[5] S. Bordács, I. Kézsmárki, D. Szaller, L. Demkó, N. Kida, H. Murakawa, Y. Onose, R. Shimano, T. Rõõm, U. Nagel, S. Miyahara, N. Furukawa, and Y. Tokura, Chirality of matter shows up via spin excitations, Nat. Phys. **8**, 734 (2012).

[6] N. Nakagawa, N. Abe, S. Toyoda, S. Kimura, J. Zaccaro, I. Gautier-Luneau, D. Luneau, Y. Kousaka, A. Sera, M. Sera, K. Inoue, J. Akimitsu, Y. Tokunaga, and T. Arima, Magneto-chiral dichroism of $CsCuCl_3$, Phys. Rev. B **96**, 121102(R) (2017).

[7] S. Mühlbauer, B. Binz, F. Jonietz, C. Pfleiderer, A. Rosch, A. Neubauer, R. Georgii, and P. Böni, Skyrmion lattice in a chiral magnet, Science **323**, 915 (2009).

[8] A. Fert, N. Reyren, and V. Cros, Magnetic skyrmions: Advances in physics and potential applications, Nat. Rev. Mater. **2**, 17031 (2017).

[9] T. Lancaster, Skyrmions in magnetic materials, Contemp. Phys. **60**, 246 (2019).

[10] D. A. Mayoh, J. Bouaziz, A. E. Hall, J. B. Staunton, M. R. Lees, and G. Balakrishnan, Giant topological and planar Hall effect in $Cr_{1/3}NbS_2$, Phys. Rev. Res. **4**, 013134 (2022).

[11] G. L. J. A. Rikken, A new twist on spintronics, Science **331**, 864 (2011).

[12] S. Emori, U. Bauer, S.-M. Ahn, E. Martinez, and G. S. Beach, Current-driven dynamics of chiral ferromagnetic domain walls, Nat. Mater. **12**, 611 (2013).

[13] K. Wang, V. Bheemarasetty, J. Duan, S. Zhou, and G. Xiao, Fundamental physics and applications of skyrmions: A review, J. Magn. Magn. Mater. **563**, 169905 (2022).

[14] H. Wang, Y. Dai, G.-M. Chow, and J. Chen, Topological Hall transport: Materials, mechanisms and potential applications, Prog. Mater. Sci. **130**, 100971 (2022).

[15] S.-W. Cheong and X. Xu, Magnetic chirality, npj Quantum Mater. **7**, 40 (2022).

[16] K. Marty, V. Simonet, E. Ressouche, R. Ballou, P. Lejay, and P. Bordet, Single domain magnetic helicity and triangular chirality in structurally enantiopure $Ba_3NbFe_3Si_2O_{14}$, Phys. Rev. Lett. **101**, 247201 (2008).

[17] R. D. Johnson, K. Cao, L. C. Chapon, F. Fabrizi, N. Perks, P. Manuel, J. J. Yang, Y. S. Oh, S.-W. Cheong, and P. G. Radaelli, $MnSb_2O_6$: A polar magnet with a chiral crystal structure, Phys. Rev. Lett. **111**, 017202 (2013).

[18] N. D. Khanh, T. Nakajima, X. Yu, S. Gao, K. Shibata, M. Hirschberger, Y. Yamasaki, H. Sagayama, H. Nakao, L. Peng, K. Nakajima, R. Takagi, T.-h. Arima, Y. Tokura, and S. Seki, Nanometric square skyrmion lattice in a centrosymmetric tetragonal magnet, Nat. Nanotechnol. **15**, 444 (2020).

[19] H. Huang and I. Affleck, Susceptibility and Dzyaloshinskii-Moriya interaction in the Haldane-gap compound $Ni(C_2H_8N_2)_2NO_2(ClO_4)$, Phys. Rev. B **69**, 184414 (2004).

[20] S. Vaidya, S. P. M. Curley, P. Manuel, J. R. Stewart, M. D. Le, C. Balz, T. Shiroka, S. J. Blundell, K. A. Wheeler, I. Calderon-Lin, Z. E. Manson, J. L. Manson, J. Singleton, T. Lancaster, R. D. Johnson, and P. A. Goddard, Magnetic properties of a staggered $S = 1$ chain with an alternating single-ion anisotropy direction, Phys. Rev. B **111**, 014421 (2025).

[21] R. Feyerherm, A. Loose, T. Ishida, T. Nogami, J. Kreitlow, D. Baabe, F. J. Litterst, S. Süllow, H.-H. Klauss, and K. Doll, Weak ferromagnetism with very large canting in a chiral lattice: $Fe(pyrimidine)_2Cl_2$, Phys. Rev. B **69**, 134427 (2004).

[22] J. Pitcairn, M. A. Ongkiko, A. Iliceto, P. J. Speakman, S. Calder, M. J. Cochran, J. A. M. Paddison, C. Liu, S. P. Argent, A. J. Morris, and M. J. Cliffe, Controlling noncollinear ferromagnetism in van der Waals metal–organic magnets, J. Am. Chem. Soc. **146**, 19146 (2024).

[23] K. Y. Povarov, L. Facheris, S. Velja, D. Blosser, Z. Yan, S. Gvasaliya, and A. Zheludev, Magnetization plateaux cascade in the frustrated quantum antiferromagnet Cs_2CoBr_4, Phys. Rev. Res. **2**, 043384 (2020).

[24] L. Facheris, S. D. Nabi, K. Y. Povarov, Z. Yan, A. G. Moshe, U. Nagel, T. Rõõm, A. Podlesnyak, E. Ressouche, K. Beauvois, J. R. Stewart, P. Manuel, D. Khalyavin, F. Orlandi, and A. Zheludev, Magnetic field induced phases and spin Hamiltonian in Cs_2CoBr_4, Phys. Rev. B **109**, 104433 (2024).

[25] S. Vaidya, A. Hernández-Melián, J. P. Tidey, S. P. M. Curley, S. Sharma, P. Manuel, C. Wang, G. L. Hannaford, S. J. Blundell, Z. E. Manson, J. L. Manson, J. Singleton, T. Lancaster, R. D. Johnson, and P. A. Goddard, Pseudo-easy-axis anisotropy in antiferromagnetic $S = 1$ diamond-lattice systems, Phys. Rev. B **110**, 174438 (2024).

[26] D. C. Dender, P. R. Hammar, D. H. Reich, C. Broholm, and G. Aeppli, Direct observation of field-induced incommensurate fluctuations in a one-dimensional $S = 1/2$ antiferromagnet, Phys. Rev. Lett. **79**, 1750 (1997).

[27] R. Feyerherm, S. Abens, D. Günther, T. Ishida, M. Meißner, M. Meschke, T. Nogami, and M. Steiner, Magnetic-field induced gap and staggered susceptibility in the $S = 1/2$ chain $[PM \cdot Cu(NO_3)_2(H_2O)_2]_n$ (PM = pyrimidine), J. Phys.: Condens. Matter **12**, 8495 (2000).

[28] B. M. Huddart, M. Gomilšek, T. J. Hicken, F. L. Pratt, S. J. Blundell, P. A. Goddard, S. J. Kaech, J. L. Manson, and T. Lancaster, Magnetic order and ballistic spin transport in a sine-Gordon spin chain, Phys. Rev. B **103**, L060405 (2021).

[29] M. Oshikawa and I. Affleck, Field-induced gap in $S = 1/2$ antiferromagnetic chains, Phys. Rev. Lett. **79**, 2883 (1997).

[30] I. Affleck and M. Oshikawa, Field-induced gap in Cu benzoate and other $S = \frac{1}{2}$ antiferromagnetic chains, Phys. Rev. B **60**, 1038 (1999).

[31] S. A. Zvyagin, A. K. Kolezhuk, J. Krzystek, and R. Feyerherm, Excitation hierarchy of the quantum sine-Gordon spin chain in a strong magnetic field, Phys. Rev. Lett. **93**, 027201 (2004).

[32] J. Liu, S. Kittaka, R. D. Johnson, T. Lancaster, J. Singleton, T. Sakakibara, Y. Kohama, J. van Tol, A. Ardavan, B. H. Williams, S. J. Blundell, Z. E. Manson, J. L. Manson, and P. A. Goddard, Unconventional field-induced spin gap in an $S = 1/2$ chiral staggered chain, Phys. Rev. Lett. **122**, 057207 (2019).

[33] See Supplemental Material at http://link.aps.org/supplemental/10.1103/2gnf-lrdx for further background and additional details on the experimental methods and sample synthesis. It also includes information on the anisotropy tensor calculations and mean-field model, which includes Refs. [20,21,25,26,29–32,44,45,47,53,55,63,69,74–91].

[34] R. Boča, Zero-field splitting in metal complexes, Coord. Chem. Rev. **248**, 757 (2004).

[35] J. L. Manson, Z. E. Manson, A. Sargent, D. Y. Villa, N. L. Etten, W. J. Blackmore, S. P. Curley, R. C. Williams, J. Brambleby, P. A. Goddard, A. Ozarowski, M. N. Wilson, B. M. Huddart, T. Lancaster, R. D. Johnson, S. J. Blundell, J. Bendix, K. A. Wheeler, S. H. Lapidus, F. Xiao, *et al.*, Enhancing easy-plane anisotropy in bespoke Ni(II) quantum magnets, Polyhedron **180**, 114379 (2020).

[36] J. M. Law, H.-J. Koo, M.-H. Whangbo, E. Brücher, V. Pomjakushin, and R. K. Kremer, Strongly correlated one-dimensional magnetic behavior of $NiTa_2O_6$, Phys. Rev. B **89**, 014423 (2014).

[37] S. Mugiraneza and A. M. Hallas, Tutorial: a beginner's guide to interpreting magnetic susceptibility data with the Curie-Weiss law, Commun. Phys. **5**, 95 (2022).

[38] O. Avenel, J. Xu, J. S. Xia, M.-F. Xu, B. Andraka, T. Lang, P. L. Moyland, W. Ni, P. J. C. Signore, C. M. C. M. van Woerkens, E. D. Adams, G. G. Ihas, M. W. Meisel, S. E. Nagler, N. S. Sullivan, Y. Takano, D. R. Talham, T. Goto, and N. Fujiwara, Low-temperature magnetic measurements of an $S = 1$ linear-chain Heisenberg antiferromagnet, Phys. Rev. B **46**, 8655 (1992).

[39] J. Law, H. Benner, and R. Kremer, Padé approximations for the magnetic susceptibilities of Heisenberg antiferromagnetic spin chains for various spin values, J. Phys.: Condens. Matter **25**, 065601 (2013).

[40] A. K. Bera, B. Lake, A. T. M. N. Islam, B. Klemke, E. Faulhaber, and J. M. Law, Field-induced magnetic ordering and single-ion anisotropy in the quasi-one-dimensional Haldane chain compound $SrNi_2V_2O_8$: A single-crystal investigation, Phys. Rev. B **87**, 224423 (2013).

[41] J. Brambleby, J. L. Manson, P. A. Goddard, M. B. Stone, R. D. Johnson, P. Manuel, J. A. Villa, C. M. Brown, H. Lu, S. Chikara, V. Zapf, S. H. Lapidus, R. Scatena, P. Macchi, Y.-S. Chen, L.-C. Wu, and J. Singleton, Combining microscopic and macroscopic probes to untangle the single-ion anisotropy and exchange energies in an $S = 1$ quantum antiferromagnet, Phys. Rev. B **95**, 134435 (2017).

[42] R. C. Williams, W. J. A. Blackmore, S. P. M. Curley, M. R. Lees, S. M. Birnbaum, J. Singleton, B. M. Huddart, T. J. Hicken, T. Lancaster, S. J. Blundell, F. Xiao, A. Ozarowski, F. L. Pratt, D. J. Voneshen, Z. Guguchia, C. Baines, J. A. Schlueter, D. Y. Villa, J. L. Manson, and P. A. Goddard, Near-ideal molecule-based Haldane spin chain, Phys. Rev. Res. **2**, 013082 (2020).

[43] A. J. Steele, T. Lancaster, S. J. Blundell, P. J. Baker, F. L. Pratt, C. Baines, M. M. Conner, H. I. Southerland, J. L. Manson, and J. A. Schlueter, Magnetic order in quasi-two-dimensional molecular magnets investigated with muon-spin relaxation, Phys. Rev. B **84**, 064412 (2011).

[44] Edited by S. J. Blundell, R. D. Renzi, T. Lancaster, and F. L. Pratt, *Muon Spectroscopy: An Introduction* (Oxford University Press, Oxford, 2022).

[45] L. C. Chapon, P. Manuel, P. G. Radaelli, C. Benson, L. Perrott, S. Ansell, N. J. Rhodes, D. Raspino, D. Duxbury, E. Spill, and J. Norris, Wish: The new powder and single crystal magnetic diffractometer on the second target station, Neutron News **22**, 22 (2011).

[46] S. Vaidya, P. Manuel, M. Coak, R. Johnson, J. Manson, and P. Goddard, Magnetic ground states of staggered and chiral integer-spin chains, STFC ISIS Neutron and Muon Source, 2022, https://doi.org/10.5286/ISIS.E.RB2210219.

[47] J. Rodríguez-Carvajal, Recent advances in magnetic structure determination by neutron powder diffraction, Physica B **192**, 55 (1993).

[48] H. T. Stokes, D. M. Hatch, and B. J. Campbell, ISODISTORT, ISOTROPY Software Suite, https://iso.byu.edu/isodistort.php.

[49] B. J. Campbell, H. T. Stokes, D. E. Tanner, and D. M. Hatch, *ISODISPLACE*: A web-based tool for exploring structural distortions, J. Appl. Crystallogr. **39**, 607 (2006).

[50] H. J. Schulz, Dynamics of coupled quantum spin chains, Phys. Rev. Lett. **77**, 2790 (1996).

[51] J. Brambleby, P. A. Goddard, R. D. Johnson, J. Liu, D. Kaminski, A. Ardavan, A. J. Steele, S. J. Blundell, T. Lancaster, P. Manuel, P. J. Baker, J. Singleton, S. G. Schwalbe, P. M. Spurgeon, H. E. Tran, P. K. Peterson, J. F. Corbey, and J. L. Manson, Magnetic ground state of the two isostructural polymeric quantum magnets $[Cu(HF_2)(pyrazine)_2]SbF_6$ and $[Co(HF_2)(pyrazine)_2]SbF_6$ investigated with neutron powder diffraction, Phys. Rev. B **92**, 134406 (2015).

[52] D. M. Pajerowski, A. P. Podlesnyak, J. Herbrych, and J. Manson, High-pressure inelastic neutron scattering study of the anisotropic $S = 1$ spin chain $Ni(HF_2)(3\text{-Clpyradine})_4]BF_4$, Phys. Rev. B **105**, 134420 (2022).

[53] R. I. Bewley, J. W. Taylor, and S. M. Bennington, LET, a cold neutron multi-disk chopper spectrometer at ISIS, Nucl. Instrum. Methods Phys. Res. Sect. A **637**, 128 (2011).

[54] S. Vaidya, R. Steward, R. Johnson, J. Manson, and P. Goddard, Measuring magnetic anisotropy and magnetic excitations in staggered and chiral spin-1 chains, STFC ISIS Neutron and Muon Source, 2023, https://doi.org/10.5286/ISIS.E.RB2310305.

[55] S. Toth and B. Lake, Linear spin wave theory for single-Q incommensurate magnetic structures, J. Phys.: Condens. Matter **27**, 166002 (2015).

[56] E. M. Wheeler, R. Coldea, E. Wawrzyńska, T. Sörgel, M. Jansen, M. M. Koza, J. Taylor, P. Adroguer, and N. Shannon, Spin dynamics of the frustrated easy-axis triangular antiferromagnet $2H\text{-}AgNiO_2$ explored by inelastic neutron scattering, Phys. Rev. B **79**, 104421 (2009).

[57] D. Dahlbom, H. Zhang, Z. Laraib, D. M. Pajerowski, K. Barros, and C. Batista, Renormalized classical theory of quantum magnets, arXiv:2304.03874.

[58] M. Songvilay, S. Petit, F. Damay, G. Roux, N. Qureshi, H. C. Walker, J. A. Rodriguez-Rivera, B. Gao, S.-W. Cheong, and C. Stock, From one- to two-magnon excitations in the $S = 3/2$ magnet $\beta - CaCr_2O_4$, Phys. Rev. Lett. **126**, 017201 (2021).

[59] J. L. Manson, D. M. Pajerowski, J. M. Donovan, B. Twamley, P. A. Goddard, R. Johnson, J. Bendix, J. Singleton, T. Lancaster, S. J. Blundell, J. Herbrych, P. J. Baker, A. J. Steele, F. L. Pratt, I. Franke-Chaudet, R. D. McDonald, A. Plonczak, and P. Manuel, Spatially anisotropic $S = 1$ square-lattice antiferromagnet with single-ion anisotropy realized in a Ni(II)pyrazine-n, n'-dioxide coordination polymer, Phys. Rev. B **108**, 094425 (2023).

[60] X. Bai, S.-S. Zhang, Z. Dun, H. Zhang, Q. Huang, H. Zhou, M. B. Stone, A. I. Kolesnikov, F. Ye, C. D. Batista, and M. Mourigal, Hybridized quadrupolar excitations in the spin-anisotropic frustrated magnet FeI_2, Nat. Phys. **17**, 467 (2021).

[61] S. Sakamoto, T. Higo, M. Shiga, K. Amemiya, S. Nakatsuji, and S. Miwa, Observation of spontaneous x-ray magnetic circular dichroism in a chiral antiferromagnet, Phys. Rev. B **104**, 134431 (2021).

[62] J. Okamoto, R.-P. Wang, Y.-Y. Chu, H.-W. Shiu, A. Singh, H.-Y. Huang, C.-Y. Mou, S. Teh, H.-T. Jeng, K. Du, X. Xu, S.-W. Cheong, C.-H. Du, C.-T. Chen, A. Fujimori, and D.-J. Huang, Giant X-ray circular dichroism in a time-reversal invariant antiferromagnet, Adv. Mater. **36**, 2309172 (2024).

[63] K. Wierschem and P. Sengupta, Quenching the Haldane gap in spin-1 Heisenberg antiferromagnets, Phys. Rev. Lett. **112**, 247203 (2014).

[64] J. A. Schlueter, H. Park, G. J. Halder, W. R. Armand, C. Dunmars, K. W. Chapman, J. L. Manson, J. Singleton, R. McDonald, A. Plonczak, J. Kang, C. Lee, M.-H. Whangbo, T. Lancaster, A. J. Steele, I. Franke, J. D. Wright, S. J. Blundell, F. L. Pratt, J. deGeorge, *et al.*, Importance of halogen $\cdots$ halogen contacts for the structural and magnetic properties of CuX_2(pyrazine-N, N'-dioxide)$(H_2O)_2$ (X = Cl and Br), Inorg. Chem. **51**, 2121 (2012).

[65] M. Cortijo, S. Herrero, R. Jimenez-Aparicio, and E. Matesanz, Modulation of the magnetic properties of two-dimensional compounds $[NiX_2(N\text{–}N)]$ by tailoring their crystal structure, Inorg. Chem. **52**, 7087 (2013).

[66] M. Cortijo, S. Herrero, R. Jimenez-Aparicio, J. Perles, J. L. Priego, and J. Torroba, Tuning of adsorption and magnetic properties in a series of self-templated isostructural Ni(II) metal-organic frameworks, Cryst. Growth Des. **14**, 716 (2014).

[67] J. Liu, P. A. Goddard, J. Singleton, J. Brambleby, F. Foronda, J. S. Möller, Y. Kohama, S. Ghannadzadeh, A. Ardavan, S. J. Blundell, T. Lancaster, F. Xiao, R. C. Williams, F. L. Pratt, P. J. Baker, K. Wierschem, S. H. Lapidus, K. H. Stone, P. W. Stephens, J. Bendix, *et al.*, Antiferromagnetism in a family of $S = 1$ square lattice coordination polymers $NiX_2(pyz)_2$ (X = Cl, Br, I, NCS; pyz = pyrazine), Inorg. Chem. **55**, 3515 (2016).

[68] M. Kubus, A. Lanza, R. Scatena, L. H. R. Dos Santos, B. Wehinger, N. Casati, C. Fiolka, L. Keller, P. Macchi, C. Rüegg, and K. W. Krämer, Quasi-2D Heisenberg antiferromagnets $[CuX(pyz)_2](BF_4)$ with X = Cl and Br, Inorg. Chem. **57**, 4934 (2018).

[69] W. J. A. Blackmore, S. P. M. Curley, R. C. Williams, S. Vaidya, J. Singleton, S. Birnbaum, A. Ozarowski, J. A. Schlueter, Y.-S. Chen, B. Gillon, A. Goukassov, I. Kibalin, D. Y. Villa, J. A. Villa, J. L. Manson, and P. A. Goddard, Magneto-structural correlations in Ni^{2+}–halide $\cdots$ halide–Ni^{2+} chains, Inorg. Chem. **61**, 141 (2022).

[70] M. J. Coak, S. P. M. Curley, Z. Hawkhead, J. P. Tidey, D. Graf, S. J. Clark, P. Sengupta, Z. E. Manson, T. Lancaster, P. A. Goddard, and J. L. Manson, Asymmetric phase diagram and dimensional crossover in a system of spin-$\frac{1}{2}$ dimers under applied hydrostatic pressure, Phys. Rev. B **108**, 224431 (2023).

[71] M. Geers, D. M. Jarvis, C. Liu, S. S. Saxena, J. Pitcairn, E. Myatt, S. A. Hallweger, S. M. Kronawitter, G. Kieslich, S. Ling, A. B. Cairns, D. Daisenberger, O. Fabelo, L. Cañadillas Delgado, and M. J. Cliffe, High-pressure behavior of the magnetic van der Waals molecular framework $Ni(NCS)_2$, Phys. Rev. B **108**, 144439 (2023).

[72] K. Y. Povarov, D. E. Graf, A. Hauspurg, S. Zherlitsyn, J. Wosnitza, T. Sakurai, H. Ohta, S. Kimura, H. Nojiri, V. O. Garlea, A. Zheludev, A. Paduan-Filho, M. Nicklas, and S. A. Zvyagin, Pressure-tuned quantum criticality in the large-D antiferromagnetic DTN, Nat. Commun. **15**, 2295 (2024).

[73] S. Vaidya *et al.*, Data for "Single-ion anisotropy driven chiral magnetism in a spin-1 antiferromagnetic chain", 2025, https://wrap.warwick.ac.uk/202033.

[74] Y. Kono, T. Sakakibara, C. P. Aoyama, C. Hotta, M. M. Turnbull, C. P. Landee, and Y. Takano, Field-induced quantum criticality and universal temperature dependence of the

magnetization of a spin-1/2 Heisenberg chain, Phys. Rev. Lett. **114**, 037202 (2015).

[75] S. Ruijsenaars, Sine-Gordon equation, in *Encyclopedia of Mathematical Physics*, edited by J.-P. Françoise, G. L. Naber, and T. S. Tsun (Academic Press, Oxford, 2006), pp. 576–583.

[76] A. F. Albuquerque, C. J. Hamer, and J. Oitmaa, Quantum phase diagram and excitations for the one-dimensional $S = 1$ Heisenberg antiferromagnet with single-ion anisotropy, Phys. Rev. B **79**, 054412 (2009).

[77] F. D. M. Haldane, Nonlinear field theory of large-spin Heisenberg antiferromagnets: Semiclassically quantized solitons of the one-dimensional easy-axis Néel state, Phys. Rev. Lett. **50**, 1153 (1983).

[78] S. Chattopadhyay, D. Jain, V. Ganesan, S. Giri, and S. Majumdar, Observation of large-D magnetic phase in Sr_3NiPtO_6, Phys. Rev. B **82**, 094431 (2010).

[79] W. J. Blackmore, J. Brambleby, T. Lancaster, S. J. Clark, R. D. Johnson, J. Singleton, A. Ozarowski, J. A. Schlueter, Y.-S. Chen, A. M. Arif, *et al.*, Determining the anisotropy and exchange parameters of polycrystalline spin-1 magnets, New J. Phys. **21**, 093025 (2019).

[80] J. L. Manson, S. H. Lapidus, P. W. Stephens, P. K. Peterson, K. E. Carreiro, H. I. Southerland, T. Lancaster, S. J. Blundell, A. J. Steele, P. A. Goddard, F. L. Pratt, J. Singleton, Y. Kohama, R. D. McDonald, R. E. Del Sesto, N. A. Smith, J. Bendix, S. A. Zvyagin, J. Kang, C. Lee, *et al.*, Structural, electronic, and magnetic properties of quasi-1D quantum magnets [Ni $(HF_2)(pyz)_2$] X (pyz = pyrazine; X = PF_6–, SbF_6–) exhibiting Ni-FHF-Ni and Ni-pyz-Ni spin interactions, Inorg. Chem. **50**, 5990 (2011).

[81] H.-L. Sun, Z.-M. Wang, and S. Gao, Strategies towards single-chain magnets, Coord. Chem. Rev. **254**, 1081 (2010).

[82] W.-X. Zhang, R. Ishikawa, B. Breedlove, and M. Yamashita, Single-chain magnets: Beyond the Glauber model, RSC Adv. **3**, 3772 (2013).

[83] V. Pianet, M. Urdampilleta, T. Colin, R. Clérac, and C. Coulon, Domain walls in single-chain magnets, Phys. Rev. B **96**, 214429 (2017).

[84] X.-T. Liu, X.-Y. Wang, W.-X. Zhang, P. Cui, and S. Gao, Weak ferromagnetism and dynamic magnetic behavior in a single end-to-end azide-bridged nickel(II) chain, Adv. Mater. **18**, 2852 (2006).

[85] G. M. Sheldrick, *SHELXT* – Integrated space-group and crystal-structure determination, Acta Crystallogr. A **71**, 3 (2015).

[86] G. M. Sheldrick, Crystal structure refinement with *SHELXL*, Acta Crystallogr. C Struct. Chem. **71**, 3 (2015).

[87] O. V. Dolomanov, L. J. Bourhis, R. J. Gildea, J. A. K. Howard, and H. Puschmann, *OLEX2*: A complete structure solution, refinement and analysis program, J. Appl. Crystallogr. **42**, 339 (2009).

[88] J. Bhattacharjee, S. Chakravarty, J. L. Richardson, and D. J. Scalapino, Some properties of a one-dimensional Ising chain with an inverse-square interaction, Phys. Rev. B **24**, 3862 (1981).

[89] S. P. Thompson, J. E. Parker, J. Potter, T. P. Hill, A. Birt, T. M. Cobb, F. Yuan, and C. C. Tang, Beamline I11 at diamond: A new instrument for high resolution powder diffraction, Rev. Sci. Instrum. **80**, 075107 (2009).

[90] J. Bezanson, A. Edelman, S. Karpinski, and V. B. Shah, Julia: A fresh approach to numerical computing, SIAM Rev. **59**, 65 (2017).

[91] J. Hannay and J. Nye, Fibonacci numerical integration on a sphere, J. Phys. A: Math. Gen. **37**, 11591 (2004).